Filtered Backprojection in Compton Imaging Using a Spherical Harmonic Wiener Filter With Pixelated CdZnTe

Daniel Shy , *Member, IEEE*, Zhuo Chen , *Graduate Student Member, IEEE*, Jeffrey A. Fessler , *Fellow, IEEE*, and Zhong He, *Senior Member, IEEE*

Abstract—Filtered backprojection is an image reconstruction technique for Compton imaging that provides reasonably high resolution at much lower computational costs when compared to iterative methods. This work applies a Wiener filter that has been derived for spherical harmonics on Compton imaging using the OrionUM pixelated CdZnTe imaging spectrometer. To regularize the filter, an investigation is made into the power spectral density of the signal and noise to develop an appropriate spectral signal-to-noise ratio model for the restoration process. Experimental measurements were conducted with two ^{228}Th sources placed 30° apart. The resulting filtered image of the two sources has an average full-width-at-half-maximum (FWHM) of 9.8° or 7.5° when using a mean squared error and structural similarity optimization approach, respectively, an improvement from the 29.0° FWHM image when using simple backprojection.

Index Terms—Filtered backprojection (FBP), gamma-ray imaging, spherical harmonics (SHs), Wiener filter.

I. INTRODUCTION

COMPTON imaging is a technique for estimating the directional origin of incoming gamma rays and has found applications in many fields such as astronomy [1] and medicine [2]. There are many image reconstruction techniques, including both iterative and noniterative methods. Filtered backprojection (FBP) offers an alternate image reconstruction technique to simple backprojection (SBP) and is advantageous in scenarios where high resolution is desired while remaining computationally cheap when compared to iterative techniques such as maximum likelihood expectation-maximization [3].

Various approaches have been developed to filter Compton images. Cree and Bones [4] derived the first inversion formula for the conical Radon transform and has been followed by other formulas with various assumptions of cone sets and

detector geometry [5]–[7]. Basko *et al.* [8] developed an analytical inversion method to reconstruct planar projections from cone surfaces via spherical harmonic (SH) expansions which can then be further filtered. Parra [9] then extended the model to use all possible scattering angles with the Klein–Nishina cross section taken into account. That approach, however, did not consider that the Compton camera is unlikely to detect the entire set of scatter angles. Therefore, Parra's technique was augmented by Tomitani and Hirasawa [10] to limit the potential angles used in the analytical point spread function (PSF). In the above studies, the filtering process was accomplished via a truncated inverse filter approach. Haefner *et al.* [11] introduced a filtering approach that places a 4π sphere in a 3-D Cartesian space and used 3-D Radon transforms to complete the filtering process with a Tikhonov regularization method.

Chu *et al.* [3] applied the Wiener filter on backprojected rings that were weighted by the probability of them occurring. The weighting scheme was applied to reduce the effects of the shift-variant PSF. We build on that work as they did not account for proper SH properties in the filter design. Next, we model a power spectral density (PSD) of the signal and noise to regularize the process. Section II overviews the OrionUM CdZnTe imaging system and Section III discusses the general imaging model. Section IV derives the Wiener filter for SHs, whereas Section V explores the behavior of the signal-to-noise ratio (SNR) that is used to regularize the filter. Section VI describes how the simulated PSF model was developed and Section VII applies the proposed technique on experimental data using a ^{228}Th source.

II. UNIVERSITY OF MICHIGAN ORIONUM 4π COMPTON IMAGER

The current University of Michigan CdZnTe platform is named OrionUM and is composed of nine $2 \times 2 \times 1.5$ cm^3 CdZnTe crystals arranged in a $3 \times 3 \times 1$ array [12]. Each crystal has a planar cathode and an 11×11 pixelated anode array with a 1.72 mm pixel pitch. The depth of interaction can be estimated using the cathode-to-anode ratio, or drift time. This allows for the 3-D position reconstruction of each interaction.

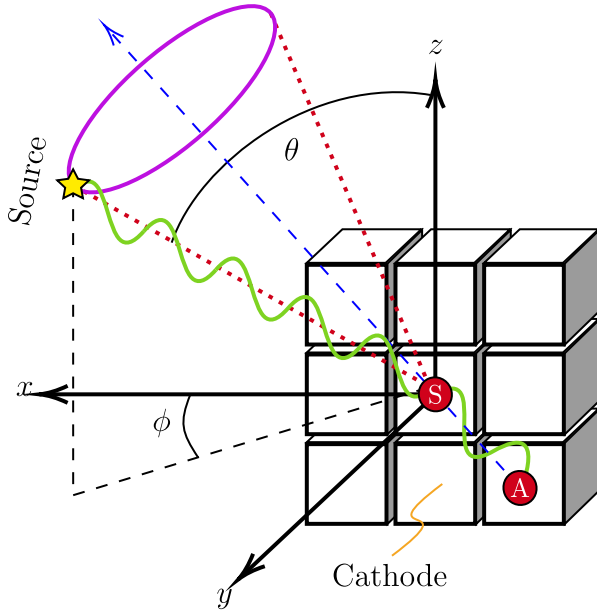This study uses the 3-MeV dynamic range mode that has a single-pixel resolution better than 0.4% full-width at half-

Fig. 1. Diagram of the $3 \times 3 \times 1$ crystal OrionUM system. The normal of the cathode is pointed toward $(90°, 90°)$, or $\hat{y}$. The diagram depicts a source with a yellow star located at (θ, ϕ) with a Compton cone (red dotted line) and Compton ring (solid purple ellipse) projected onto it. The gamma ray is emitted from the source, scatters in a location labeled with a "S" red dot, and then absorbed in the location labeled by the "A" red dot. The green squiggly line portrays the gamma-ray's trajectory. The blue dashed arrow represents the lever arm and is a vector from "A" to "S." The spacing between each crystal is 2.5 cm center-to-center from the neighboring crystal.

maximum (FWHM) at 662 keV, which is a degradation from 0.35% when using the 700-keV dynamic range.

Fig. 1 illustrates the coordinate system along with the detector layout. The detector's isocenter, which is normal to the cathode, is located at $(\theta, \phi) = (90°, 90°)$.

III. INTRODUCTION TO FILTERED BACKPROJECTION

A general linear model for Compton imaging measurements can be made as

$$\mathbb{E}[\underline{o}] = \mathbf{T}\mathbf{f} \tag{1}$$

where $\mathbf{f}$ is the unknown true source vector of length J that is to be estimated, $\mathbb{E}[\underline{o}]$ is the expected observation vector of length I, and $\mathbf{T}$ is an $I \times J$-sized system matrix. For "binned mode" data, I is the number of detection bins.

A. Simple Backprojection

The SBP process can be modeled as

$$\hat{\mathbf{f}}^{\text{SBP}} = \mathbf{T}'\underline{o}. \tag{2}$$

The apostrophe $'$ represents the transpose of the matrix. We are interested in analyzing the PSF of this method by examining its expectation

$$\mathbb{E}[\mathbf{f}^{\text{SBP}}] = \mathbf{T}'\mathbb{E}[\underline{o}] = \mathbf{T}'\mathbf{T}\mathbf{f} = \mathbf{B}\mathbf{f} \tag{3}$$

where $\mathbf{B} = \mathbf{T}'\mathbf{T}$ and represents the $J \times J$ matrix of PSFs. In $\mathbf{B}$, the jth column is the PSF for a source located in the jth image pixel. However, in most imaging systems including OrionUM,

$\mathbf{T}$ is not an orthogonal matrix yielding a biased SBP estimator as $\mathbf{T}'\mathbf{T} = \mathbf{B} \neq \mathbf{I}$ and does not provide a shift-invariant PSF, where $\mathbf{I}$ represents an identity matrix. Section VI discusses the construction of $\mathbf{B}$.

B. Filtered Backprojection

FBP is designed to recover the true signal by removing the blur and noise introduced by the measurement system [13]. An example is the inverse filter, used in Compton imaging by Parra [9], Xu and He [14], and Lee et al. [15]. Using the model described in (2), the SBP image can be filtered as

$$\hat{\mathbf{f}}^{\text{FBP}} = \mathbf{B}^{-1}\hat{\mathbf{f}}^{\text{SBP}}. \tag{4}$$

We analyze the PSF of the filtered image with the expectation

$$\mathbb{E}[\mathbf{f}^{\text{FBP}}] = \mathbf{B}^{-1}\mathbb{E}[\mathbf{f}^{\text{SBP}}] = \mathbf{B}^{-1}\mathbf{T}'\mathbf{T}\mathbf{f} = \mathbf{f}. \tag{5}$$

The structure of $\mathbf{T}$ implies that each row is a Compton cone in the image space. Therefore, $\mathbf{T}$ is a very large matrix as there is a huge number of possible interaction permutations a gamma ray can undertake while being attenuated in the detector. Therefore, we use list-mode reconstruction techniques to construct the observation matrix.

In practice, filtering with $\mathbf{B}^{-1}$ could amplify noise when $\mathbf{B}$ has very small values. Therefore, an advanced filter is required to perform a more practical reconstruction. This work uses the Weiner filter, which is designed to minimize the mean square error (MSE) during the restoration process [16].

IV. FILTERED BACKPROJECTION USING A SPHERICAL HARMONIC WIENER FILTER

SHs can be used to define a function $f(\theta, \phi) = f(\Omega)$ on a 4π spherical surface using a set of basis functions and therefore present a natural choice with which to perform the filtering processes for far-field Compton imaging. The SHs $Y_l^m(\Omega)$ are a function of degree l and order m. For each degree, there are $2l + 1$ orders with range $-l \leq m \leq l$. The following represents an orthonormalized SH function:

$$Y_l^m(\Omega) = \sqrt{\frac{(2l+1)}{4\pi} \cdot \frac{(l-m)!}{(l+m)!}} P_l^m(\cos\theta)e^{im\phi}. \tag{6}$$

There are three main components to the SH. First, the square root term represents the normalization element. This study uses the orthonormalized SH such that $\langle Y_{l'}^{m'}|Y_l^m\rangle = \delta_{l-l'}\delta_{m-m'}$, where $\delta_{l-l'}$ is the Kronecker delta. The second component, $P_l^m(\cos\theta)$, is the associated Legendre polynomial [17]. The last component is a complex exponential. There are many different normalizations [18], each with different properties.

Similar to the Fourier series, a transform could be made from the spherical function space to spectral space with

$$F_l^m = \int_\Omega d\Omega f(\Omega)Y_l^{m*}(\Omega) \tag{7}$$

where Y_l^{m*} represents the complex conjugate of Y_l^m. The inverse transform is defined by

$$f(\Omega) = \sum_{l=0}^{\infty} \sum_{m=-l}^{l} F_l^m Y_l^m(\Omega). \tag{8}$$

A. Notes on SHs

Convolution (⊛) in spherical space differs from that in Fourier space [19]. First, the kernel ($k(\Omega)$) in the convolution must be circularly symmetric about the North Pole ($\theta = 0$). Next, the SH transform (SHT) of the convolution is

$$\text{SHT}\{f(\Omega) \circledast k(\Omega)\} = 2\pi\sqrt{\frac{4\pi}{2l+1}}F_l^m K_l^0 \tag{9}$$

where capital letters describe the SHT of spherical functions presented in lower case. Note the loss of order for (K_l^0) which is the SHT$\{k(\Omega)\} = K_l^m$ with $m = 0$. Appendix A presents a further discussion on convolution in SHs and expands on the circularly symmetric convolution kernel.

SHs are also Hermitian functions with the following property [20]:

$$Y_l^{-m} = (-1)^l \left(Y_l^m\right)^*. \tag{10}$$

Therefore, only $m \geq 0$ SH coefficients are presented in this study. The toolbox utilized to complete the SHTs is the SHTns library [21].

B. SH Wiener Filtering

The objective of the Wiener filter (g) is to estimate the original signal $f(\Omega)$ by a linear convolution method that minimizes the mean squared error

$$\text{MSE} = \mathbb{E}\big[|f(\Omega) - \hat{f}^{\text{FBP}}(\Omega))|^2\big] \tag{11}$$

where the estimated signal is modeled as $\hat{f}^{\text{FBP}}(\Omega) = (\hat{f}^{\text{SBP}} \circledast g)(\Omega)$. The blurred observed image is modeled as $\hat{f}^{\text{SBP}} = (f \circledast h)(\Omega) + n(\Omega)$, with h denoting the PSF and n the additive noise. Next, Parseval's Theorem (25) is used to convert the estimated FBP image to SHs

$$\hat{F}_{l,m}^{\text{FBP}} = 2\pi\sqrt{\frac{4\pi}{2l+1}}G_l\hat{F}_{l,m}^{\text{SBP}} \tag{12}$$

where $\hat{F}_{l,m}^{\text{SBP}}$ and $\hat{F}_{l,m}^{\text{FBP}}$ are the SHT of the image estimates using simple and FBP techniques, respectively, and G_l is the SHT of the Wiener filter that deblurs the SBP image with the following form:

$$G_l = \frac{H_l^*}{\frac{2(2\pi)^3}{2l+1}|H_l|^2 + R_l^{-1}}; \quad R_l^{-1} = \frac{N_l^{\text{PSD}}}{S_l^{\text{PSD}}} \tag{13}$$

where S_l^{PSD} and N_l^{PSD} denote the power spectral density as a function of l and H_l denotes the SHT of the PSF. Next, R_l^{-1} represents a regularizer that is related to the inverse of the spectral-signal to spectral-noise ratio, which Section V further discusses.

Note the $2(2\pi)^3/(2l + 1)$ factor in the denominator that represents the main difference between the filter derived for Fourier space and SHs. Appendix B derives the SHs' Wiener filter, whereas Appendix C discusses Parseval's theorem.

V. MODELING OF THE SNR REGULARIZER

The regularizer in the Wiener filter is often referred to as the inverse of the SNR. It is a function of the object being imaged and the characteristics of the environment and system.
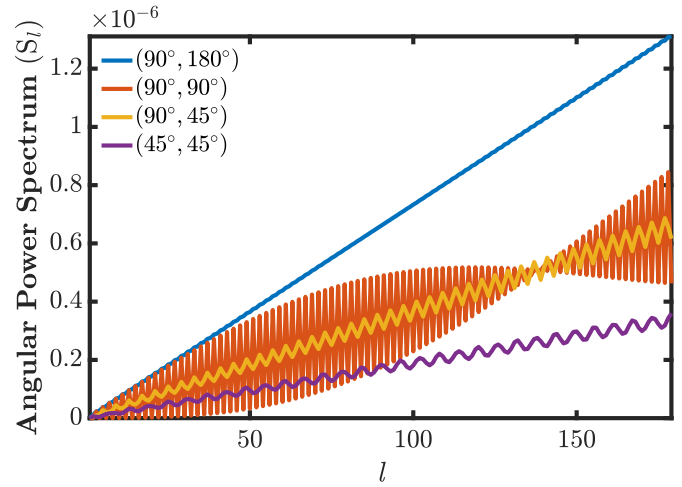

Fig. 2. Power spectra of delta impulses located in different positions on the sphere all exhibiting a nearly linear trend with degree l. Note that only $m \geq 0$ are considered here.

In this study, it represents the inverse ratio of the PSD of the signal S_l^{PSD} and noise N_l^{PSD}, modeled as

$$S_l^{\text{PSD}} = Q_l\sum_{m=-l}^{l}|F_l^m|^2; \quad N_l^{\text{PSD}} = Q_l\sum_{m=-l}^{l}|N_l^m|^2 \tag{14}$$

where Q_l represents the inner product of the SHs (1 in this study). Note that there are multiple definitions of the PSD in SHs. Liu *et al.* [22] included a $1/(2l + 1)$ factor to normalize the summation over all orders m, whereas others do not [18]. The definition in (14) arises from convenience when deriving the Wiener filter (see Appendix B). This section details the model chosen for the power spectra to formulate the regularizer.

A. Modeling of the Signal PSD (S_l^{PSD})

From (14), the power spectrum is related to the object being measured, $f(\Omega)$. This spectrum could be modeled after the true object if prior information is available, but presents a challenge when the source is unknown. Therefore, several spectral responses were calculated for Kronecker delta impulses at different locations. Fig. 2 plots them and presents a nearly linear trend as a function of degree l. We, therefore, model the PSD of the signal to be linear as follows:

$$S_l^{\text{PSD}} = c_s l \tag{15}$$

where c_s is a constant that is a function of the source intensity and distribution. Although the plots only represent power spectral densities of point sources, they can be applied to more complex sources as SHs exhibit additive linearity property [23]. Therefore, we model the PSD of the signal as a linear combination of those linear PSDs.

B. Modeling of the Noise PSD (N_l^{PSD})

The noise in this study is referred to as additive noise present in the observed signal $\hat{f}^{\text{SBP}}(\Omega)$ and we model it as "white." In SHs, there exist several interpretations of white noise. In some geophysics applications, a signal is white if
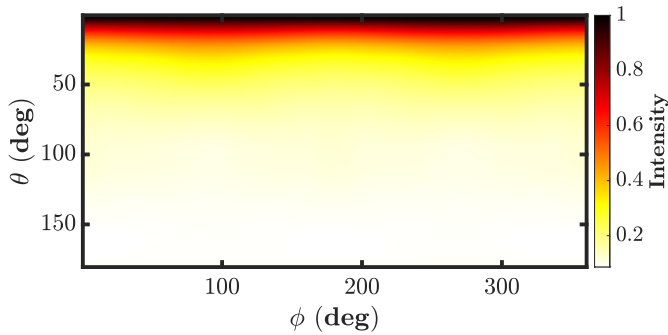
Fig. 3. SBP image of a simulated 2.6 MeV point source located at the North Pole of a single $2 \times 2 \times 2$ cm^3 crystal. This image is used as the PSF model in the filtering process.

the average power is constant for every degree of freedom (l, m) [24]. There, $N_l^m = \sigma$, where σ is a constant representative of noise in the system and results in a power spectrum that is scaled by $(2l + 1)$. Another interpretation [25] is that the spectral power is constant in l, and we choose to model the noise as such in this study

$$N_l^{\text{PSD}} = \sigma. \tag{16}$$

C. Ratio of the Signal and Noise Power Spectral Densities

In summary, the signal power spectrum is assumed to be a linear function of l in this study, whereas the noise is assumed to be white and constant through l. Taking the ratio between the two assumptions gives

$$R_l^{-1} = \frac{N_l^{\text{PSD}}}{S_l^{\text{PSD}}} = \frac{\sigma}{c_s l} = \frac{c}{l} \tag{17}$$

where c is a constant determined via an optimization process described in Section VII. The implications of (17) entail that the filter will attenuate the signal more heavily for larger degrees l.

VI. POINT SPREAD FUNCTION MODEL

The PSF is the image response to a given point source. There exist several techniques to model the PSF [3], [9], [10], [14], [26]. This study models the PSF from a Geant4 simulation [27]. A 2.6-MeV point source was modeled in the North Pole of a single $2 \times 2 \times 2$ cm^3 crystal, which was chosen to reduce the effects of the shift-variant PSF. Fig. 3 presents the reconstructed SBP image. As noted before, we assume that the PSF is shift-invariant even though the OrionUM does not have that property.

Fig. 4 shows an SHT of the SBP image and that it is mainly composed of zonal SHs (SH with $m = 0$). Due to the nature of spherical convolution, where the convolution kernel is required to be circularly symmetric about the North Pole, we model the PSF with only zonal SHs. This function is then stored in memory and is used during the filtering process. In principle, the modeled PSF can also be a function of energy to account for the different physical processes in different energies.

VII. RESULTS FROM APPLYING THE FILTER

This section presents results from an experimental measurement using the OrionUM detector system and a 20 μCi ^{228}Th source, which emits a 2.6-MeV gamma ray. The experiment
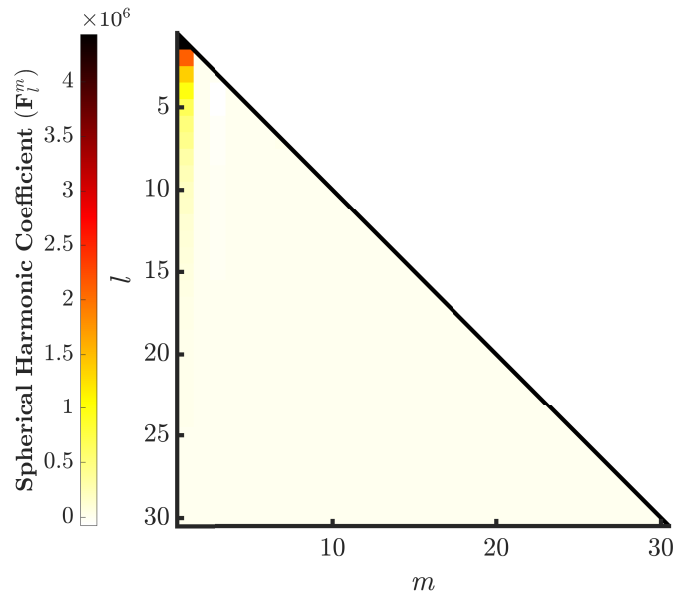

Fig. 4. SHT of the SBP image for a source at the North Pole that is presented in Fig. 3. Note that the most significant coefficients are zonal and only the first 30° are presented.

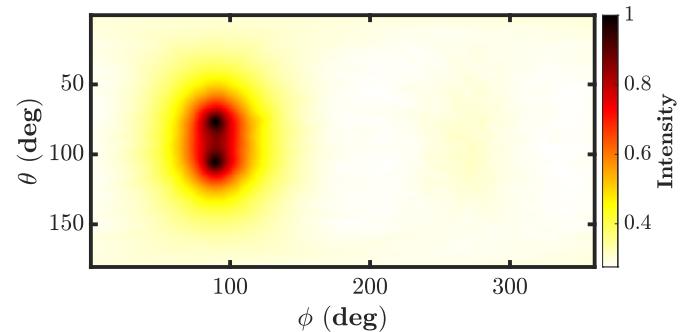Fig. 5. SBP of two ^{228}Th check sources placed 15° above and below the isocenter of the detector.

involved placing the same source 85 cm away from the isocenter and offset 22.8 cm from it at two different times, as two sources of equal intensity were not available. This implies that there is a 30° separation between them when placed at $(75°, 90°)$ and $(105°, 90°)$. Each measurement location culminated in a six-day measurement, and the two data sets were concatenated to emulate a two-source setup.

Fig. 5 presents an SBP using energies between 2.55 and 2.69 MeV and utilized only two- and three-pixel events. Side-neighboring events were removed and events with an opening angle less than 50° were cut as they might represent pair production, charge sharing, or events with Bremsstrahlung X-rays [28]. Composed of 1.24×10^5 events, the average FWHM of the SBP image is about 29.0°, as calculated via a double Gaussian fit of the bi-modal distribution when considering $\phi = 90° \pm 1$. The averaged FWHM is referred to as the mean FWHM of each of the two sources. Fig. 6 presents the spherical harmonic transform of the SBP image.

A. Filtered Backprojection

When applying the Wiener filter in the spectral space, there is an associated regularizer that is tied to the SNR of
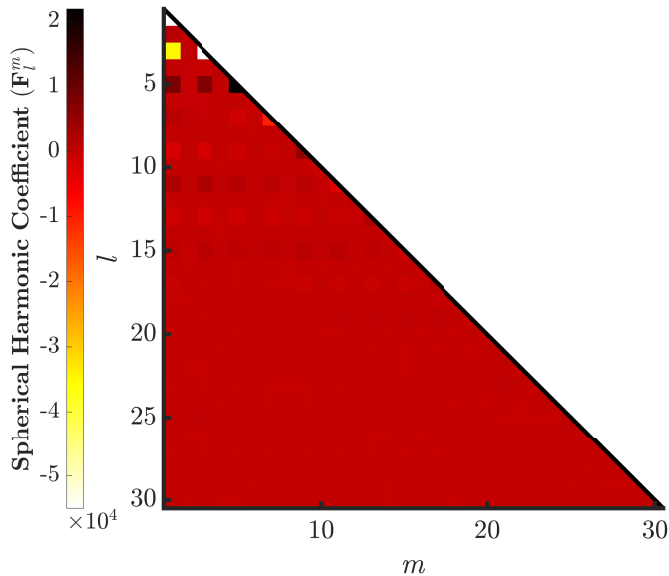
Fig. 6. SHT of Fig. 5. Note that the $l = 0$ SH is removed from this plot as it is the "breathing" harmonic and represents a dc offset.
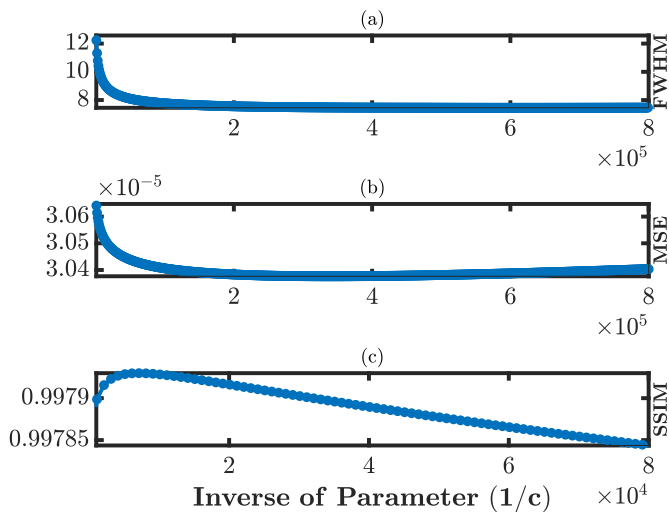

Fig. 7. Image metrics associated with the filtering process displaying (a) FWHM, (b) mean squared error (MSE), and (c) SSIM for different $1/c$ values.

the measurement. In this study, the optimized parameter [c from (15)] is identified by the value that provides the best MSE or structural similarity (SSIM) [29]. The SSIM image metric was applied as an index to measure the SSIM of two images (the estimated and true image) with the addition of perception-based metrics by accounting for pixel interdependencies [29]. The parameter c is iterated through and the image metrics are calculated with a synthetic reference where two Kronecker deltas are modeled at each of the source locations.

Fig. 7 presents the image metrics associated with the reconstructed images. The x-axis in the plots is associated with the inverse of the slope parameter ($1/c$). The FWHM plot, which is the average of the two peaks calculated via geometric interpolation, presents the resolution improving with larger ($1/c$) and plateauing to around $7.5°$.

TABLE I
IMAGE METRIC RESULTS FROM THE TWO-SOURCE EXPERIMENT

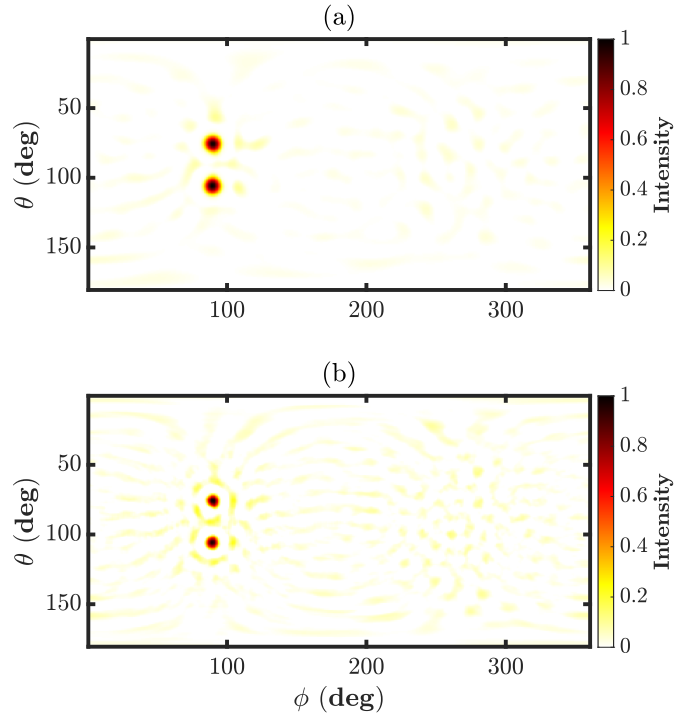| Technique	$1/c$	FWHM°	MSE $\times 10^{-5}$	SSIM
SBP	$\sim$	29.0	3.14	0.9909
SSIM (FBP)	7,000	9.8	3.06	0.9979
MSE (FBP)	339,100	7.5	3.04	0.9976

Fig. 8. FBP images as optimized using (a) SSIM and (b) MSE criteria.

With lessened regularization, the Wiener filter will percolate the spectra at larger degrees and produce a high-frequency noise. Therefore, additional image metrics were considered, such as the mean squared error that has optimized the filter with a $1/c = 3.3 \times 10^5$ to result in an FWHM of $7.5°$. The SSIM index, which takes additional metrics into account to quantify structural patterns, selects a parameter of $1/c = 7000$ and results in an FWHM of $9.8°$. Table I summarizes the different image metrics calculated for each optimization technique.

Fig. 8 plots the SSIM- and MSE-optimized images, whereas Fig. 9 plots the power spectral densities of the resulting images. As SSIM takes structured noise into account, it is perhaps more conservative in the filtering process, which is visible when comparing Fig. 8(a) and (b). The MSE-optimized image yields more ringing structures emanating and surrounding the two sources. The MSE-optimized image, however, produces a higher resolution image, with an average FWHM of $7.5°$. Fig. 10 presents the SH coefficients of the filtered image when using the SSIM maximization criteria.

VIII. DISCUSSION

A. Shift Variant PSF

This work does not address issues arising from the shift-variant nature of the PSF, a property that the Wiener filter
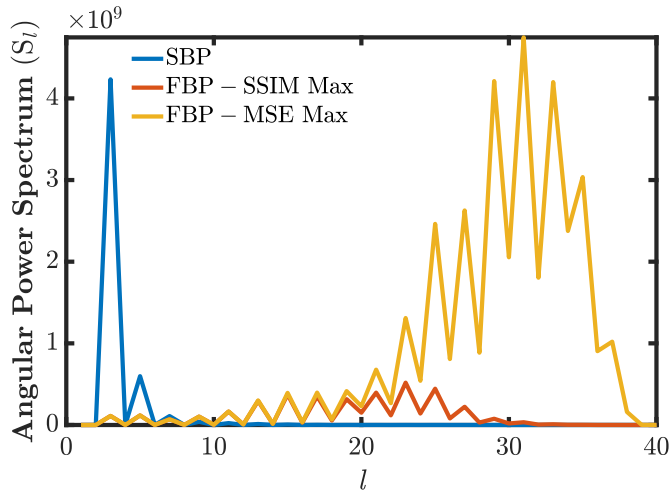
Fig. 9.   PSDs of the SBP and FBP optimized with the different optimization criteria.

Source Location	θ FWHM°	ϕ FWHM°
$(90°, 90°)$	20.2	20.1
$(90°, 135°)$	19.5	23.6
$(90°, 180°)$	17.4	30.9

process, we do not expect results to be fiercely different for extended sources. If different counting statistics were to be used, the inverse SNR regularizer should scale appropriately. Adaptive parameters could be developed that model the counting statistics that will select the optimized regularization parameters.

If there were to be multiple sources in the field of view with different intensities, the filter will attempt to reconstruct the minimized mean squared error of all the sources. However, if one wishes to develop a locally optimized image for a single source, then a more adaptive filter may be desired. One could also achieve this by reconstructing images on partial spheres resulting in interesting future work on partial sphere convolutions.

Further investigation is required to model actual noise characteristics of the imager and its Poisson nature as it may not be white. Finally, all the analyses in this work were done for a stationary camera. One should give careful consideration to the coordinates should the work be applied to a mobile camera.

IX. CONCLUSION

This work applies a Wiener filter that was derived for SHs in Compton imaging on the OrionUM pixelated CdZnTe detector. In the process, the power spectral densities of the signal and noise were modeled to regularize the filter during the reconstruction process. Experimental measurements using two ^{228}Th sources placed 30° apart resulted in a filtered image with an average FWHM resolution of 9.8° and 7.5° when using an MSE and SSIM optimization approach, respectively. This is down from the 29.0° FWHM when using SBP.
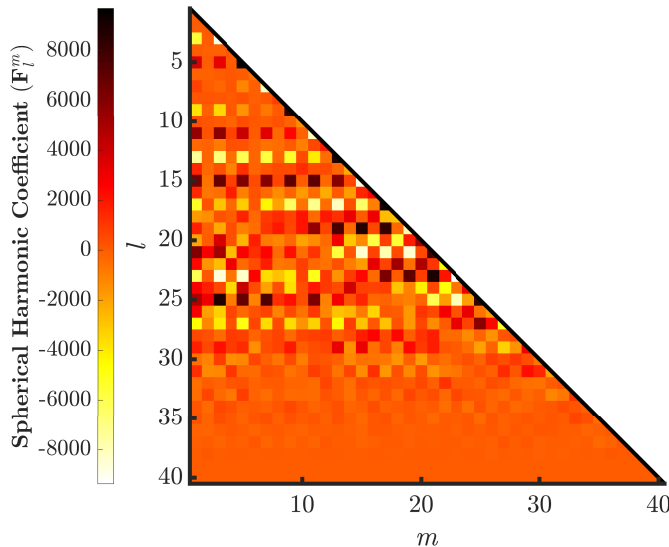

Fig. 10.   SH coefficients of an FBP image using the SSIM maximization criteria.

cannot accommodate. Moreover, the convolution process in SHs requires a circularly symmetric convolution kernel. However, the OrionUM system and perhaps other imagers experience local shift invariance. So sources near a localized region, especially near the isocenter of the detector, do not experience great PSF deformation. Fig. 8 shows this when the sources are 15° off the isocenter as the reconstructed sources are very circular.

Table II indexes the FWHM values associated with the azimuth and the altitude of sources located at various locations using simulated 2.6 MeV data. This demonstrates the shift-variant nature of the OrionUM detector. The "acceptability" of using the shift-invariant assumption should be based on the user's desired tolerance level.

APPENDIX A
ADDITIONAL NOTES ON CONVOLUTION IN SHS

Convolution is a mathematical operation that modifies a function with a kernel to express the amount of overlap between the two [30]. Given by the "Convolution Theorem," the Fourier transform of the convolution of two functions in the time or Euclidean domain is simply the product of their respective Fourier transforms [23].

The comparable SH convolution for functions on the 2-D sphere differs from that in Euclidean space. It takes the form

$$\text{SHT}\{f(\Omega) \circledast k(\Omega)\} = 2\pi \sqrt{\frac{4\pi}{2l+1}} F_l^m K_l^0 \qquad (18)$$

where ($\circledast$) represents the convolution operator, $f(\Omega)$ and $k(\Omega)$ represent the function and convolution kernel on the sphere,

B. Future Work for More Complex Sources

The proposed filter is designed to provide the minimized mean squared error of the signal. Since FBP is a linear

respectively, whereas the capital letters reflect their SHT. The major difference is the additional term that is a function of order l and the fact that the kernel is reduced to only zonal components K_l^0. Note that the convolution in (18) is for orthonormalized SHs.

A. Invalidity of the Standard Convolution Theorem in SHs

The first difference between the Fourier and SH case is the $2\pi\sqrt{4\pi/(2l+1)}$ term which originates from the Funk–Hecke theorem [20], [31]. This implies that the standard Convolution Theorem does not apply in SH

$$(f \circledast k)(\Omega) \neq \text{SHT}^{-1}\{\text{SHT}\{f(\Omega)\} \cdot \text{SHT}\{k(\Omega)\}\}. \quad (19)$$

B. Circular Symmetric Convolution Kernel (K_l^0)

In (18), the kernel ($k(\Omega)$) loses all $m \neq 0$ components and becomes "zonal" (K_l^0). A function composed of only zonal SHs is circularly symmetric about the North Pole [32]. This symmetry can be seen as a surface of revolution, where a function is traced out in the intensity-θ plane and rotated about the $\hat{z}$-axis/North Pole over all ϕ. Therefore, latitudinal lines represent isolines. If the kernel $k(\Omega)$ is not circularly symmetric, such convolution would yield a poor result. In this work, the kernel is the Wiener filter, G_l in (12).

Fig. 3 presents an example of a near-circularly invariant function by projecting the image of a source placed in the North Pole. Fig. 4 presents the SHT of Fig. 3 and is mainly composed of zonal SHs with minimal influence from $m \neq 0$ SHs.

The reduction to a zonal kernel implies that convolution in SH is not commutative ($f(\Omega) \circledast k(\Omega) \neq k(\Omega) \circledast f(\Omega)$). Therefore, an assumption must be made that one of the elements is zonal and circularly symmetric over the North Pole. A derivation of the SH convolution theorem is available in Theorem 2 of Driscoll and Healy [19].

APPENDIX B
DERIVATION OF THE WIENER FILTER FOR THE SH CASE

This section derives the Wiener Filter [16] for deconvolution in SH space. We begin with the following definitions:

$$\hat{f}^{\text{SBP}} = (f \circledast h)(\Omega) + n(\Omega)$$
$$\hat{f}^{\text{FBP}}(\Omega) = (\hat{f}^{\text{SBP}} \circledast g)(\Omega) \quad (20)$$

where $f(\Omega)$ is the object being imaged, $\hat{f}^{\text{SBP}}$ and $\hat{f}^{\text{FBP}}$ are the SBP and filtered estimates, respectively, $h(\Omega)$ is the blurring impulse function, and $n(\Omega)$ is the additive noise. The goal is to recover the signal via deconvolution with filter $g(\Omega)$. The convolutions are conducted such that the convolution kernel is the Wiener filter.

Convolution in SHs can be accomplished as

$$\text{SHT}\{f(\Omega) \circledast h(\Omega)\} = M_l F_l^m H_l^0. \quad (21)$$

The M_l coefficient for an orthonormalized SH is [19]

$$M_l = 2\pi\sqrt{\frac{4\pi}{2l+1}}. \quad (22)$$

Therefore, the SHT of (20) is

$$\hat{F}_{l,m}^{\text{SBP}} = M_l H_l F_l^m + N_l^m$$
$$\hat{F}_{l,m}^{\text{FBP}} = M_l G_l F_{l,m}^{\text{SBP}}$$
$$= M_l G_l [M_l H_l F_l^m + N_l^m]. \quad (23)$$

The objective of the Wiener filter is ($\hat{F}_{l,m}^{\text{FBP}}$) to estimate the original signal (F_l^m) with a filter that minimizes the mean squared error

$$\text{MSE} = \mathbb{E}[|f(\Omega) - \hat{f}^{\text{FBP}}(\Omega))|^2]. \quad (24)$$

Next, we utilize Parseval's Theorem [33] in SH [34]

$$\int_\Omega |f(\Omega)|^2 d\Omega = \sum_{l=0}^\infty Q_l \sum_{m=-l}^l |F_l^m|^2 \quad (25)$$

where Q_l is a factor that is dependent on the normalization of the SHs. Appendix C derives (25).

In the following transform of the MSE, the l subscript is removed for all the variables that do not have an order m dependence, and $\hat{F}_{l,m}^{\text{FBP}}$ is shortened to $\hat{F}_l^m$. The MSE in terms of (l, m) is

$$= \sum_{l=0}^\infty \left[Q_l \sum_{m=-l}^l |F_l^m - \hat{F}_l^m|^2 \right]$$
$$= \sum_{l=0}^\infty \left[Q_l \sum_{m=-l}^l |F_l^m|^2 - F_l^m \hat{F}_l^{m*} - F_l^{m*} \hat{F}_l^m + |\hat{F}_l^m|^2 \right]$$

plugging in the definition for $\hat{F}_{l,m}^{\text{FBP}}$ from (23), we continue with

$$= \sum_{l=0}^\infty \left[Q_l \sum_{m=-l}^l |F_l^m|^2 - F_l^m [M^2 GH F_l^m + MGN_l^m]^* \right.$$
$$- F_l^{m*} [M^2 GH F_l^m + MGN_l^m] + |M^2 GH F_l^m|^2$$
$$+ MGH F_l^m [MGN_l^m]^* + [MGH F_l^m]^* MGN_l^m$$
$$\left. + |MGN_l^m|^2 \right].$$

We assume that the noise is independent of the signal

$$\mathbb{E}[F_l^m N_l^{m*}] = \mathbb{E}[F_l^{m*} N_l^m] = 0$$

and continue with the MSE derivation

$$= \sum_{l=0}^\infty \left[Q_l \sum_{m=-l}^l |F_l^m|^2 - F_l^m [M^2 GH F_l^m]^* \right.$$
$$\left. - F_l^{m*} [M^2 GH F_l^m] + |M^2 GH F_l^m|^2 + |MGN_l^m|^2 \right].$$

Let $S_l^{\text{PSD}} = Q_l \sum_{m=-l}^l |F_l^m|^2$ and $N_l^{\text{PSD}} = Q_l \sum_{m=-l}^l |N_l^m|^2$ represent the power spectrum for the signal and noise, respectively. We remind ourselves that the objective of the Wiener filter is to minimize the MSE. In this case, we will want to derive G_l such that it minimizes the MSE for a given l. As several variables might be complex, including G_l, define the complex function $G_l = G_l^r + i G_l^i$ and take the derivative

of the MSE derivation with respect to the real and complex parts and set them equal to zero

$$G_l^r = \frac{S_l^{\mathrm{PSD}}\,\mathrm{Re}\{H\}}{M^2 H^2 S_l + N_l^{\mathrm{PSD}}}$$

$$G_l^i = -\frac{S_l^{\mathrm{PSD}}\,\mathrm{Im}\{H\}}{M^2 H^2 S_l + N_l^{\mathrm{PSD}}}.$$

We, therefore, can solve for the final Wiener filter in SHs by adding the real and complex components

$$G_l = \frac{H_l^*}{\frac{2(2\pi)^3}{2l+1}|H_l|^2 + R_l^{-1}} \qquad (26)$$

with $R_l^{-1} = \frac{N_l^{\mathrm{PSD}}}{S_l^{\mathrm{PSD}}}$. The filtered image is therefore

$$\hat{F}_{l,m}^{\mathrm{FBP}} = 2\pi\sqrt{\frac{4\pi}{2l+1}}\, G_l \hat{F}_{l,m}^{\mathrm{SBP}}$$

$$= 2\pi\sqrt{\frac{4\pi}{2l+1}}\,\frac{H_l^*}{\frac{2(2\pi)^3}{2l+1}|H_l|^2 + R_l^{-1}}\hat{F}_{l,m}^{\mathrm{SBP}}. \qquad (27)$$

APPENDIX C
DERIVATION OF THE PARSEVAL'S THEOREM IN THE SH CASE

Parseval's theorem slightly differs for SH and the chosen normalization. Let us start with the integral of the square of the function

$$\int_\Omega |f(\Omega)|^2 \mathrm{d}\Omega. \qquad (28)$$

We use (8) for the following derivation:

$$\int_\Omega |f(\Omega)|^2 \mathrm{d}\Omega = \int_\Omega |\sum_{l=0}^\infty \sum_{m=-l}^l F_l^m Y_l^m(\Omega)|^2 \mathrm{d}\Omega$$

$$= \int_\Omega |\sum_{l=0}^\infty F_l^{-l} Y_l^{-l} + F_l^{-l+1} Y_l^{-l+1}$$

$$+ F_l^{-l+2} Y_l^{-l+2} + \cdots + F_l^l Y_l^l|^2 \mathrm{d}\Omega$$

$$= \int_\Omega |F_0^0\, Y_0^0 + F_1^{-1} Y_1^{-1} + F_1^0 Y_1^0$$

$$+ F_1^1\, Y_1^1 + \cdots + F_l^l Y_l^l|^2 \mathrm{d}\Omega.$$

Next, we expand the quadratic and remind ourselves of the following orthogonality identity:

$$\int_\Omega Y_{l'}^{m'*}(\Omega) Y_l^m(\Omega) \mathrm{d}\Omega = Q_l \delta_{l-l'} \delta_{m-m'} \qquad (29)$$

where Q_l is a factor that depends on the chosen SH normalization. Therefore, all elements $l' \neq l$ and $m' \neq m$ will be zeroed (as they are all orthogonal). All we are left with is

$$= \left[Q_l |F_0^0|^2 + Q_l |F_1^{-1}|^2 + Q_l |F_1^0|^2 + Q_l |F_1^1|^2 + \cdots \right]$$

$$= \sum_{l=0}^\infty Q_l \sum_{m=-l}^l |F_l^m|^2.$$

Therefore, Parseval's theorem for SHs is

$$\int_\Omega |f(\Omega)|^2 \mathrm{d}\Omega = \sum_{l=0}^\infty Q_l \sum_{m=-l}^l |F_l^m|^2. \qquad (30)$$

ACKNOWLEDGMENT

REFERENCES

[1] V. Schönfelder, A. Hirner, and K. Schneider, "A telescope for soft gamma ray astronomy," *Nucl. Instrum. Meth.*, vol. 107, no. 2, pp. 385–394, 1973. [Online]. Available: http://www.sciencedirect.com/science/article/pii/0029554X73902577

[2] E. Draeger *et al.*, "3D prompt gamma imaging for proton beam range verification," *Phys. Med. Biol.*, vol. 63, no. 3, Jan. 2018, Art. no. 035019.

[3] J. Chu, M. Streicher, J. A. Fessler, and Z. He, "Unbiased filtered back-projection in 4π Compton imaging with 3D position sensitive detectors," *IEEE Trans. Nucl. Sci.*, vol. 63, no. 6, pp. 2750–2756, Dec. 2016.

[4] M. J. Cree and P. J. Bones, "Towards direct reconstruction from a gamma camera based on Compton scattering," *IEEE Trans. Med. Imag.*, vol. 13, no. 2, pp. 398–407, Jun. 1994.

[5] F. Terzioglu, "Some inversion formulas for the cone transform," *Inverse Problems*, vol. 31, no. 11, Oct. 2015, Art. no. 115010. [Online]. Available: https://doi.org/10.1088%2F0266-5611%2F31%2F11%2F115010

[6] S. Moon, "Inversion of the conical Radon transform with vertices on a surface of revolution arising in an application of a Compton camera," *Inverse Problems*, vol. 33, no. 6, Apr. 2017, Art. no. 065002. [Online]. Available: https://doi.org/10.1088%2F1361-6420%2Faa69c9

[7] V. Maxim, "Filtered backprojection reconstruction and redundancy in Compton camera imaging," *IEEE Trans. Image Process.*, vol. 23, no. 1, pp. 332–341, Jan. 2014.

[8] R. Basko, G. L. Zeng, and G. T. Gullberg, "Application of spherical harmonics to image reconstruction for the Compton camera," *Phys. Med. Biol.*, vol. 43, no. 4, pp. 887–894, Apr. 1998. [Online]. Available: https://doi.org/10.1088%2F0031-9155%2F43%2F4%2F016

[9] L. C. Parra, "Reconstruction of cone-beam projections from Compton scattered data," *IEEE Trans. Nucl. Sci.*, vol. 47, no. 4, pp. 1543–1550, Aug. 2000.

[10] T. Tomitani and M. Hirasawa, "Image reconstruction from limited angle Compton camera data," *Phys. Med.Biol.*, vol. 47, no. 12, pp. 2129–2145, Jun. 2002. [Online]. Available: https://doi.org/10.1088%2F0031-9155%2F47%2F12%2F309

[11] A. Haefner, D. Gunter, R. Barnowski, and K. Vetter, "A filtered back-projection algorithm for 4π Compton camera data," *IEEE Trans. Nucl. Sci.*, vol. 62, no. 4, pp. 1911–1917, Aug. 2015.

[12] J. Xia, "Interaction reconstruction in digital 3-D CdZnTe under various circumstances," Ph.D. dissertation, Dept. Nucl. Eng. Radiol. Sci., Univ. Michigan, Ann Arbor, MI, USA, 2019. [Online]. Available: http://cztlab.engin.umich.edu/wp-content/uploads/sites/187/2019/09/jiaweix_1.pdf

[13] H. Barrett and W. Swindell, *Radiological Imaging: The Theory of Image Formation, Detection, and Processing*. Amsterdam, The Netherlands: Elsevier, Dec. 2012.

[14] D. Xu and Z. He, "Filtered back-projection in 4π Compton imaging with a single 3D position sensitive CdZnTe detector," *IEEE Trans. Nucl. Sci.*, vol. 53, pp. 2787–2796, 2006.

[15] T. Lee, H. Lee, Y. Kim, and W. Lee, "Estimation of Compton imager using single 3D position-sensitive LYSO scintillator: Monte Carlo simulation," *J. Korean Phys. Soc.*, vol. 71, no. 2, pp. 70–76, Jul. 2017.

[16] N. Wiener, *Extrapolation, Interpolation, and Smoothing of Stationary Time Series*. Cambridge, MA, USA: MIT Press, 1964.

[17] W. Thomson and P. G. Tait, *Treatise Natural Philosophy* (Cambridge Library Collection-Mathematics), vol. 1, 2nd ed. Cambridge, U.K.: Cambridge Univ. Press, 1883.

[18] M. A. Wieczorek and M. Meschede, "SHTools: Tools for working with spherical harmonics," *Geochemistry, Geophysics, Geosystems*, vol. 19, no. 8, pp. 2574–2592, Aug. 2018. [Online]. Available: https://agupubs.onlinelibrary.wiley.com/doi/abs/10.1029/2018GC007529

[19] J. R. Driscoll and D. M. Healy, "Computing Fourier transforms and convolutions on the 2-Sphere," *Adv. Appl. Math.*, vol. 15, no. 2, pp. 202–250, Jun. 1994. [Online]. Available: http://www.sciencedirect.com/science/article/pii/S0196885884710086

[20] J. D. Jackson, *Classical Electrodynamics*, 2nd ed. New York, NY, USA: Wiley, 1975.

[21] N. Schaeffer, "Efficient spherical harmonic transforms aimed at pseudospectral numerical simulations," *Geochem., Geophys., Geosyst.*, vol. 14, no. 3, pp. 751–758, Mar. 2013. [Online]. Available: https://agupubs.onlinelibrary.wiley.com/doi/abs/10.1002/ggge.20071

[22] A. Liu, Y. Zhang, and A. R. Parsons, "Spherical harmonic analyses of intensity mapping power spectra," *Astrophys. J.*, vol. 833, no. 2, p. 242, Dec. 2016. [Online]. Available: https://doi.org/10.3847%2F1538-4357%2F833%2F2%2F242

[23] A. Macovski, *Medical Imaging Systems* (Prentice-Hall Information and System Sciences Series). Upper Saddle River, NJ, USA: Prentice-Hall, 1983.

[24] R. G. Hipkin, "The statistics of pink noise on a sphere: Applications to mantle density anomalies," *Geophys. J. Int.*, vol. 144, no. 2, pp. 259–270, Feb. 2001, doi: 10.1046/j.0956-540X.2000.01327.x.

[25] F. A. Dahlen and F. J. Simons, "Spectral estimation on a sphere in geophysics and cosmology," *Geophys. J. Int.*, vol. 174, no. 3, pp. 774–807, Sep. 2008, doi: 10.1111/j.1365-246X.2008.03854.x.

[26] M. Hirasawa and T. Tomitani, "Effect of compensation for scattering angular uncertainty in analytical Compton camera reconstruction," *Phys. Med. Biol.*, vol. 49, no. 10, pp. 2083–2093, May 2004. [Online]. Available: https://doi.org/10.1088%2F0031-9155%2F49%2F10%2F017

[27] J. Allison *et al.*, "Recent developments in Geant4," *Nucl. Instrum. Meth. Phys. Res. A, Accel., Spectrometers, Detectors Associated Equip.*, vol. 835, pp. 186–225, Nov. 2016. [Online]. Available: http://www.sciencedirect.com/science/article/pii/S0168900216306957

[28] D. Shy, J. Xia, and Z. He, "Artifacts in high-energy Compton imaging with 3-D position-sensitive CdZnTe," *IEEE Trans. Nucl. Sci.*, vol. 67, no. 8, pp. 1920–1928, Aug. 2020.

[29] Z. Wang, A. C. Bovik, H. R. Sheikh, and E. P. Simoncelli, "Image quality assessment: From error visibility to structural similarity," *IEEE Trans. Image Process.*, vol. 13, no. 4, pp. 600–612, Apr. 2004. [Online]. Available: http://www.cns.nyu.edu/pub/lcv/wang03-preprint.pdf

[30] E. W. Weisstein. *Convolution*. Wolfram MathWorld. Accessed: Dec. 15, 2020. [Online]. Available: https://mathworld.wolfram.com/Convolution.html

[31] R. Basri and D. W. Jacobs, "Lambertian reflectance and linear subspaces," *IEEE Trans. Pattern Anal. Mach. Intell.*, vol. 25, no. 2, pp. 218–233, Feb. 2003.

[32] E. W. Weisstein. *Zonal Harmonic*. Wolfram MathWorld. Accessed: Dec. 15, 2020. [Online]. Available: https://mathworld.wolfram.com/ZonalHarmonic.html

[33] M.-A. Parseval des Chenes, "Memoire sur les series et sur l'integration complete d'une equation aux differences partielles lineaire du second ordre, a coefficients constants," *Memoires Presentes a l'Institut des Sci., Lettres et Arts, par Divers Savants, et lus dans ses Assemblees. Sci., Mathematiques et Physiques*, vol. 1, pp. 638–648, 1806.

[34] B. Borden and J. Luscombe, *Essential Mathematics for the Physical Sciences*. San Rafael, CA, USA: Morgan & Claypool, 2017, doi: 10.1088/978-1-6817-4485-8.